Additive Manufacturing 72 (2023) 103636

Contents lists available at ScienceDirect

Additive Manufacturing

journal homepage: www.elsevier.com/locate/addma

Understanding the process-microstructure-property relationships in material extrusion additive manufacturing of polylactic acid microcellular foams

Karun Kalia, Amir Ameli *

Department of Plastics Engineering, University of Massachusetts Lowell, 1 University Ave, Lowell, MA 01854, USA

ARTICLE INFO

Keywords:
Microcellular materials
Foams
Material extrusion additive manufacturing
Residence time
Temperature

ABSTRACT

Process-microstructure-property relationships are reported for microcellular foams printed via material extrusion (MEX) additive manufacturing (AM) process. Polylactic acid and thermally expandable microspheres were mixed and extruded to prepare the filament. In situ foaming during MEX AM process was then conducted to investigate the impact of nozzle temperature, flow rate, and print speed on the cellular morphology, mesostructure, part density, and the mechanical behavior of the foams. The temperature and the residence time were identified as the two key factors governing the foaming behavior and thus the resultant microstructure and properties. Too excessive temperature and residence time resulted in the deformed, wrinkled, or collapsed microspheres due to gas loss and contraction. On the other hand, too low temperature and residence time caused limited number of microspheres to expand, due to insufficient energy and time. Both overly activated and partially unexpanded microspheres provided nonuniform cellular morphologies and higher densities and thus adversely affected the tensile properties. The foam expansion/shrinkage behavior during the MEX AM process was demonstrated as a function of a combined process variable that unifies temperature, flow rate, and print speed. Upon the utilization of the optimum process variables, foam samples with uniform morphology, low density, and high toughness were achieved. The results shed light on the understanding and advancing of MEX AM process as a novel manufacturing approach to produce quality foams.

1. Introduction

Polymeric foams are lightweight materials that have wide range of applications in insulation, packaging, cushioning, safety, biomedical, etc. [1–8]. Thermoplastic foams are usually made using physical [1,8,9] or chemical [10–12] blowing agents. Recently, thermally expandable microspheres (TEMs), which are essentially physical blowing agents confined by a thermoplastic shell [13–15] have also been used for foaming. Injection molding [16–22] and extrusion [1,23,24] are relatively mature manufacturing technologies that are commonly used to produce thermoplastic foams.

Material extrusion (MEX) additive manufacturing (AM) usually works with thermoplastic materials and offer some key benefits compared to subtractive processes such as machining and forming processes such as injection molding and extrusion [25]. In MEX AM method, three dimensional parts, including relatively complex shapes, are made progressively by the deposition of a molten continuous bead that follows a tool path, generated based on the part design. Integrating MEX AM and polymer foaming may offer several benefits: a) low material usage, b) complex lightweight parts, c) microstructure control, c) mitigation of warpage and inter-bead voids, and d) structural customization via functionally graded foams. The manufacturing of foams through MEX AM is, however, a relatively new and emerging field.

Three different ways have been reported to make foams in MEX AM: a) pre-foaming, b) post-foaming [26–28], and c) in situ foaming [29–36]. In situ foaming, which is called foam 3D printing (F-3DP) hereafter, synchronizes the material extrusion, expansion, and deposition and there is no pre- or post-process steps required for foam expansion. In F-3DP, an expandable filament is used as the feedstock and during the printing process, foam expansion occurs by providing proper printing process conditions. The use of gas [29,30,34] and chemical blowing agents [31,35] has been reported. In both cases, the gas needs to be dissolved in the polymer melt in order to provide an acceptable level of cell nucleation. Unlike the traditional physical and chemical blowing

---

* Corresponding author.
E-mail address: Amir_Ameli@uml.edu (A. Ameli).

https://doi.org/10.1016/j.addma.2023.103636
Received 17 February 2023; Received in revised form 1 May 2023; Accepted 31 May 2023

agents, the blowing agent (gas) does not need to be dissolved in the polymer melt, which simplifies the foaming process and makes it feasible with any commercial MEX AM machine, without further modification. TEM-assisted foaming has also been examined in extrusion foaming and foam injection molding processes and the results indicate that a more uniform cellular morphology is obtainable with TEMs as opposed to other blowing agents [14,15]. The bulk density and microcellular structure may be controlled via the amount of TEM loading as well as the printing process parameters.

There are few reports on TEM-assisted F-3DP process [32,37]. Andersson et al. reported the F-3DP of polylactic acid (PLA). Their report shows a nonuniform cellular morphology with large variations in densities [32]. Pawar et al. reported the F-3DP of thermoplastic elastomer polyamide (TPE-A) [37]. They analyzed the density of the printed sample as a function of the nozzle temperature, nozzle diameter and layer height. The authors also recently reported the fabrication of expandable PLA filaments with various TEM loadings and plasticizers and demonstrated the feasibility of fabricating highly uniform cellular morphologies with good dimensional stability in printed foams [38,39].

While there has been an increasing interest in F-3DP recently, a deeper understanding of the key print process parameters that control the mesostructure, cellular morphology, and dimensional stability as well as the performance of the resultant foams is still lacking in the literature. There has been numerous studies on regular MEX AM process indicating that the printing parameters play a critical role on determining the print quality, inter-layer bond strength, and final mechanical properties of un-foamed printed parts [40–43]. Understanding and quantification of such process-microstructure-properties correlations in F-3DP process is still missing.

In this study, first a TEM masterbatch was mixed with a model matrix material, i.e., PLA to fabricate expandable filaments using single screw extrusion process, assuring that the foam expansion is suppressed during filament fabrication process. The expandable filament was then employed as the feedstock for MEX AM to 3D print the microcellular foams. To systematically study the process-microstructure-properties relationships, three key print process factors, namely, the temperature on nozzle, the melt flow rate at the nozzle exit, and the velocity of print head (print speed) were investigated. Nozzle temperature levels were selected based on the temperature window overlap between the TEM expansion and the PLA melt processing requirements. The flow rate and print speed levels were also selected based on the foam manufacturability. Tensile bars were printed at various print process conditions. The impact of F-3DP process variables on the microcellular morphology, part density, and tensile properties of the foams were investigated in detail. The foam expansion and contraction were also quantified and discussed with respect to temperature, residence time, and a combined process variable, that unifies all three process variables into one factor.

2. Experimental

2.1. Materials

The model polymer examined here was PLA (NatureWorks, Ingeo 4043D) with a density of 1.24 g.cm^{-3} and a flow rate of 6 g per 10 min at 210 °C under 2.16 kg load. For blowing agent, a TEM masterbatch from Sekisui (Advancell P501E1) was used. Tri-ethyl citrate (TEC) was also used as a plasticizer. The TEC was purchased from Sigma Aldrich (W308307) and had a molecular weight of 276.28 g.mol^{-1}. According to Sekisui, TEM P501E1 is a masterbatch containing 50 wt% TEM and 50 wt% polyethylene carrier. The microsphere's initial particle size is 21–31 μm with a bulk density of about 1.10 g.cm^{-3}. The expansion start and maximum temperatures of the TEMs are 160–180 °C and 210–230 °C, respectively. The density of TEM particles can be as low as 0.01–0.03 g.cm^{-3} once they are fully activated. More details about the TEM can found in [38]. TEC plasticizer [44] at 2 wt% was also added to the PLA/2.5 wt%TEM formulation to tailor the viscosity during filament extrusion.

2.2. Filament fabrication

An extruder, Dr. Collin E30P was used to melt blend PLA, TEC at 2.0 wt%, and TEM at 2.5 wt% for preparing the filament. The extruder had a screw diameter of 30 mm and a length of 750 mm giving an aspect ratio of 25. The screw profile consisted of Maddock/Igel elements at the end for better mixing [45–47]. Barrel temperatures were kept in between 155 and 127 °C with a screw rotational speed of 6 rpm. This resulted in a melt temperature of 161 ± 2 °C and a pressure of 20.5 ± 0.5 MPa before the die exit. More details about the filament preparation can be found in [39].

2.3. Material extrusion additive manufacturing of foams

2.3.1. Foam 3D printing process

Fig. 1(a) schematically depicts the in situ F-3DP process. Expandable filament was fed into the heater block assembly at a certain filament feed in velocity (U_I). The heater block assembly moved at the print speed of U_P. Heater block assembly includes the heater block and the nozzle, i.

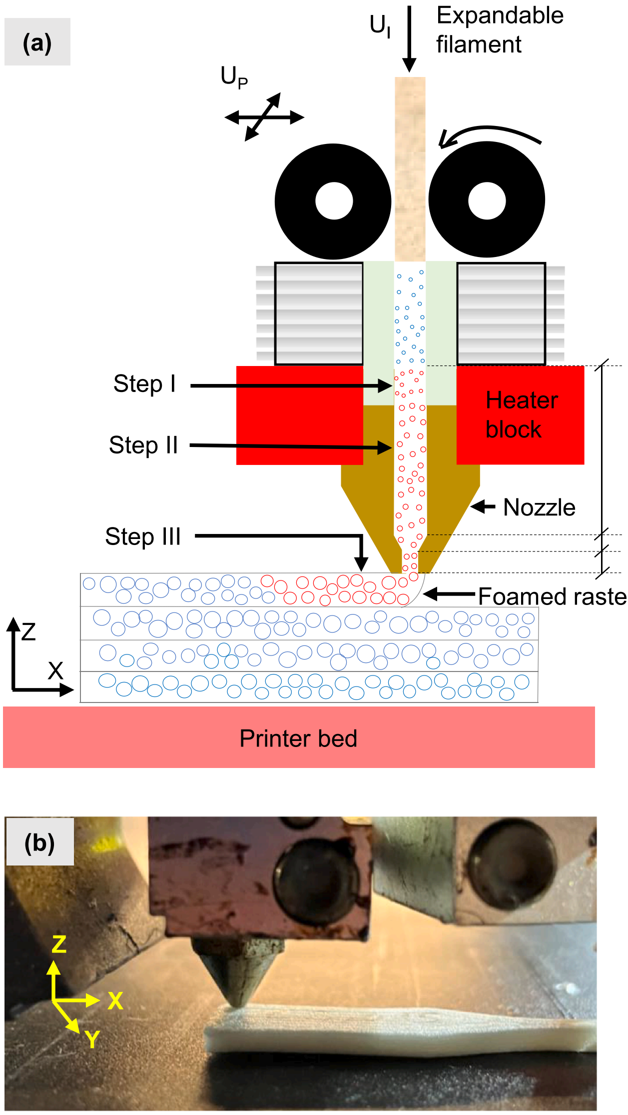

Fig. 1. (a) Schematic representation of F-3DP process and (b) an isometric view of foam printing process in action making a tensile bar. The dimensions in (a) are not to scale.

e., where the material will be in its molten state (Fig. 1(a)). The three steps of in situ F-3DP process are represented in Fig. 1(a). Step I denotes the heating stage, i.e., the TEM particles are heated up but the temperature is not yet sufficiently high to trigger the expansion. Step II denotes the initiation stage where TEM particles are hot enough to initiate the expansion as they flow toward the nozzle exit. The amount of expansion in this stage will depend on the nozzle pressure, the true temperature of the TEMs, and the residence time. In step III, the TEM particles continue growing as they exit the nozzle until the melt cools down below the minimum expansion temperature of the TEMs where the cellular morphology starts to stabilize. Fig. 1(b) shows F-3DP process in action making a tensile bar. The dimensions of the printed tensile bars were selected based on the ASTM D638 type-V specimen [48]) and the slicing of CAD model was carried out using Ideamaker to generate the tool path. A commercial 3D printer (Raise 3D Pro2) was utilized to make the foamed samples.

2.3.2. *Design of experiments*

Table 1 shows the experimental runs to investigate the impact of F-3DP process variables. The lowest nozzle temperature was selected as 175 °C which is close to the TEM's expansion start temperature while the highest nozzle temperature was set to 225 °C which is close to TEM's expansion maximum temperature. Also, the selected nozzle temperatures were within the processing temperature window of PLA. Preliminary trials also revealed that both flow rate and print head speed significantly affect the foaming behavior. Therefore, they were selected as variable factors. 100 % flow rate, which is typical in solid part printing, was used as the highest level and 55 % was selected as the lowest level. Below 55 % flow rate, incomplete prints were observed. Print speed was also examined at its widest possible range of 5–125 mm.s^{-1}. The other process parameters were kept unchanged. Nozzle diameter, raster width, layer height, infill percentage, print orientation, and bed temperature were set to 0.8 mm, 0.8 mm, 0.3 mm, 100 %, 0 °, and 55 °C, respectively.

2.3.3. *Residence time estimation*

The residence time, t_r of the material inside the heater block assembly was identified as one of the fundamental factors governing the foaming behavior and the process-microstructure relations. Therefore, t_r in each experimental run was estimated using both analytical and experimental methods. In analytical approach, Eq. (1) was used to calculate t_r:

$$t_r = \sum_{i=1}^{3} \frac{l_i}{U_i} = \frac{l_1}{U_I} + \frac{l_2}{U_C} + \frac{l_3}{U_E} \tag{1}$$

where l_1, l_2, and l_3 are the travel distances (mm) inside the heater block assembly and nozzle, as shown in Fig. 1. l_1, l_2, and l_3 were directly measured from the hotend and nozzle assembly. U_I and U_E are the filament feed in velocity and nozzle exit linear velocity (mm.s^{-1}), respectively. U_c is the average linear velocity of melt traveling through the connical section of the nozzle, which is calculated based on the U_I and U_E. U_I is calculated using the set flow rate (*FR*) as:

Table 1
The design of experiment (one factor at a time) used in the F-3DP process.

No.	Nozzle temperature (°C)	Flow rate (%)	Print head speed (mm.s^{-1})
1	175	85	25
2	200	85	25
3	225	85	25
4	200	55	25
5	200	100	25
6	200	85	5
7	200	85	125

$$U_I = \frac{\dot{Q}}{\frac{\pi}{4} d_f^2} \tag{2}$$

$$\dot{Q} = \alpha \bullet FR \tag{3}$$

$\dot{Q}$ (mm^3.s^{-1}) and d_f (mm) are the volumetric flow rate and diameter of the filament, respectively. *FR* (%) is the printer input flow rate in percentage and α is a fator that convert the flow rate from % to mm^3.s^{-1} and it is obtained from the g-code, which takes into account the other fixed print parameters. U_E is then calculated based on U_I and the ratio of the filament and nozzle diamerters using:

$$U_E = U_I \frac{d_f^2}{d_n^2} \tag{4}$$

where d_n (mm) is the nozzle diameter. When the print speed, *PS* (mm.s^{-1}) is varied, the following Eq. relates the filament feed in velocity (U_I) and *PS*:

$$U_I = \beta \bullet PS \tag{5}$$

where β is a factor obtained from the g-code, taking the other fixed printing conditions such as flow rate and nozzle diameter into account. Therefore, Eqs. (1)–(5) provides a method to calculate the residence time once input flow rate or print speed is changed. In the experimental method, the t_r values were estimated by directly measuring the time that filament took to pass from the heater block assembly and nozzle. As further discussed in Section 3.2.2, the theoretical and experimental t_r values matched relatively well, indicating that the obtained time values were reliable.

2.4. *Characterizations*

2.4.1. *Density*

A density kit (Mettler Toledo MS303TS/00) was used to obtain the density of the filament and the 3D printed parts following the ASTM D792 standard procedure [49]. The density samples of the printed foams were cut from the tensile bars. At least three samples of each condition were used in the density measurements.

2.4.2. *Microscopy*

A scanning electron microscope, SEM (JEOL JSM 6390) was utilized to study the cellular morphology of the printed tensile specimens. Micrographs of the microstructures were taken at several magnifications with an acceleration voltage of about 5 kV. Before scanning, the samples were cryo-fractured using liquid nitrogen and then coated with Au using a sputter coater (Denton vacuum sputter coater).

2.4.3. *Cell density and cell size*

The cell density and cell size of the foams were obtained by image processing of the SEM micrographs using MIPAR software. At least three hundred cell counts of each micrograph were used in the calculations of the cell density. The diameter of the same cells was also measured and used to obtain the cell size in each case. Cell density, *N* (number of cells per cm^3) was calculated using Eq. [17]:

$$N = \left(\frac{n}{A}\right)^{\frac{3}{2}} \tag{6}$$

where *n* is the number of cells, observed within a certain area, *A* (in cm^2) of SEM micrographs. Eq. 6 first calculates the 2D (surface) population density of cells by counting the number of cells observed in a certain area (cm*cm) of SEM micrograph and then extends that to 3D (volumetric) population density of the cells assuming that the cell distribution is isotropic. It is also noted the cell population density was not normalized with respect to the sample's density before foaming. Three different printed samples were considered in calculating the means and the provided error bars in the graphs denote the standard deviations.

2.4.4. *Tensile testing*

The mechanical testing of the foams was conducted by loading the specimens in tension following the ASTM D638 [48]. A displacemnt controlled load frame (Instron 5966 with 10 kN load cell) with a crosshead speed of 10 mm.min^{-1} was utilized for the testing. At least four specimens were tested for each experimental run and the tensile yield strength, tensile modulus, strain-at-break, and toughness are reported.

3. Results and discussion

3.1. *Effect of nozzle temperature*

3.1.1. *Microstructure vs. nozzle temperature*

Fig. 2(a-c) shows the internal microstructure of the printed foams at the nozzle temperatures of 175 °C, 200 °C, and 225 °C. It can be clearly seen from Fig. 2(a1–2) that at 175 °C, the inter-bead gaps and boundaries (shown with yellow arrows in Fig. 2(a-1)) were formed along with the traces of unexpanded microspheres (shown with yellow arrows in Fig. 2(a-2)). However, with an increase in the nozzle temperature to 200 °C, the inter-bead gaps vanished, and the printed foam exhibited a uniform cellular morphology with no marks of rastering (Fig. 2(b1–2)). Further increase of the nozzle temperature to 225 °C showed anomalies such as deformed TEM particles (shown with yellow arrows in Fig. 2(c-2)) and wrinkles on the TEM shell (shown with red arrows in Fig. 2(c-2, c-3). Furthermore, as shown by blue arrows in Fig. 2(a-3, b-3, c-3), the TEM shell thickness decreased as the nozzle temperature was increased, indicating that the TEMs expanded to a greater degree as the temperature was increased. The fact that the final stabilized cell sizes do not appear to be the largest in the case of 225 °C is related to the TEM shrinkage and wrinkle formation after excessive expansion, as explained later.

The relation between the temperature and the foaming behavior can be considered in two aspects, i.e., the pressure generated inside the TEMs by liquid/gas phase change and the polymer viscoelastic behavior. As the temperature rises, the heat transfer between the nozzle and the material will occur at higher rates and the internal energy of the melt will be greater. These will result in the rise of the gas pressure inside the TEMs to higher levels and with faster rates, which will ultimately cause a greater number of TEMs to activate and grow to higher degrees of expansion. In addition, the polymer viscosity in the molten state will decrease with temperature, following an Arrhenius type relation, $\eta = A \exp(\frac{E_a}{RT})$, where η is the viscosity, E_a is the activation energy, R is the Boltzmann's constant and T is the temperature. With a decrease in viscosity, polymer chain mobility will increase, which will thereby lower the matrix resistance to TEM expansion. Moreover, the TEM shell's modulus of elasticity will decrease as the temperature increases, allowing for deformation under lower force levels, which will further

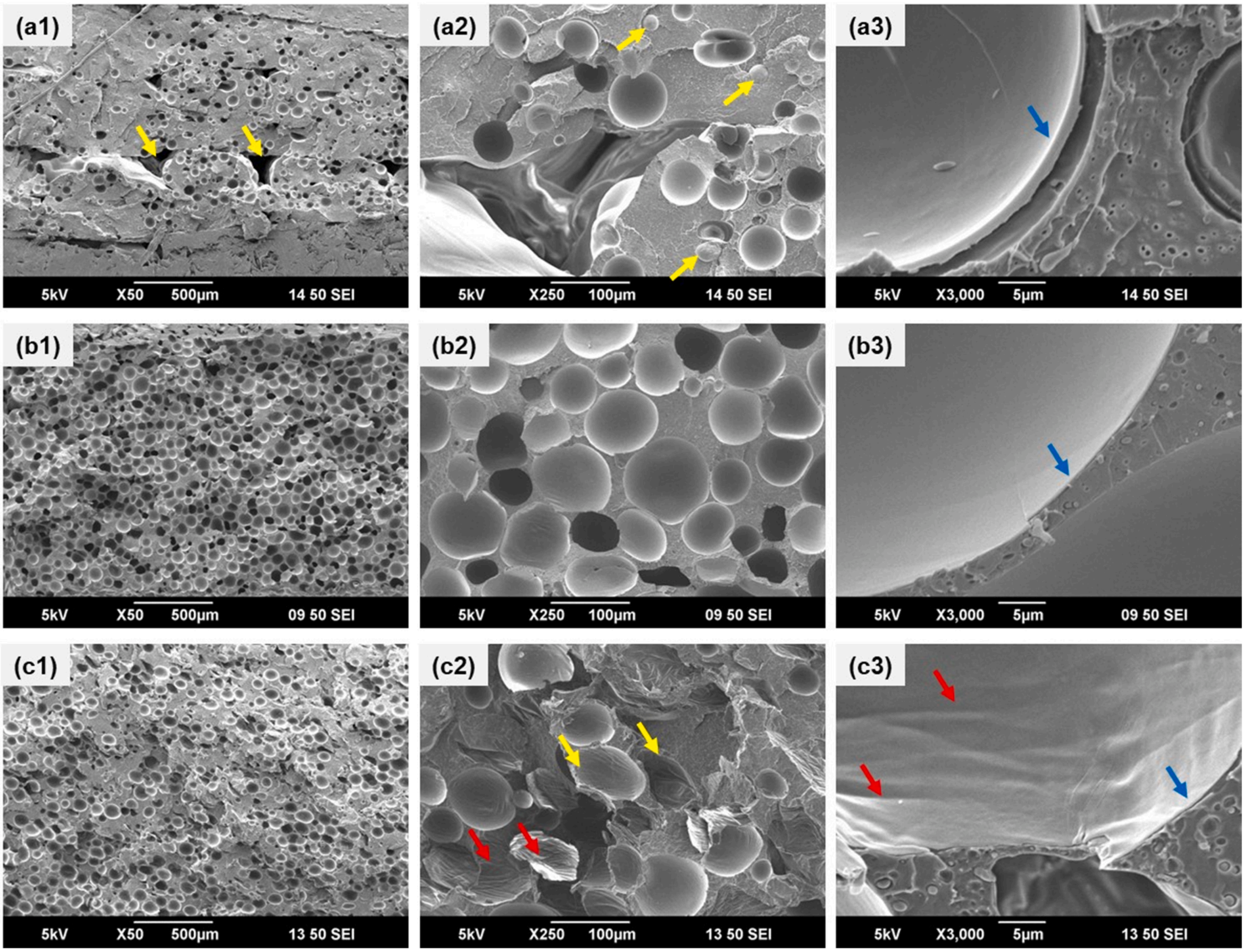

Fig. 2. Cellular morphologies of the foams printed at the nozzle temperatures of (a) 175 °C, (b) 200 °C, and (c) 225 °C. Images of 1, 2, 3 in each row were taken at three different magnifications of 50, 250 and 3000, respectively, from the same samples. The flow rate and print speed were 85 % and 25 mm.s^{-1}, respectively.

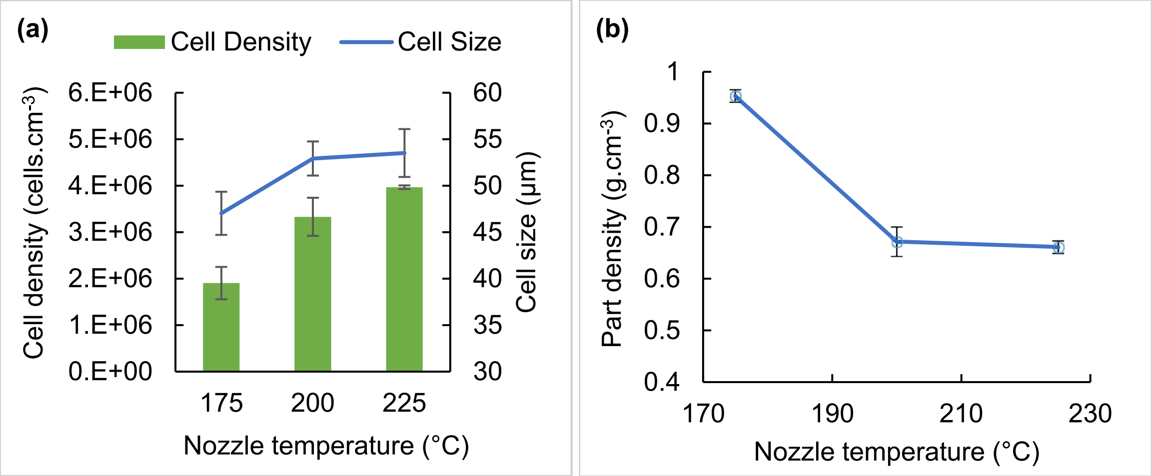

Fig. 3. (a) Cell density and cell size and (b) density of the printed foams vs. nozzle temperature. The flow rate and print speed were 85 % and 25 mm.s^{-1}, respectively.

ease the expansion.

It should be however noted that the excessively high temperatures will also be detrimental to the foaming behavior, causing contracted and/or deformed cells and defective shells. Elongated cells at high levels of temperature could be attributed to the excessive softening of the shell material and consequently its deformation due to the applied shear stresses as the melt flows. The wrinkles created on the shells could also be due to the shrinkage of the excessively expanded TEM microsphere [50,51]. If the temperature is too high, the pressure of the gas inside the TEM will also be high and thus the gas will attempt to diffuse out of the shell to lower the internal pressure [51]. Since the shell is bound to the matrix melt, it cannot freely shrink back as the gas is diffusing out and thus it creates wrinkle marks as it contracts [51].

Fig. 3(a) shows the cell size and cell density of the foams printed at various nozzle temperatures. At 175 °C, cell density and cell size were found to be the lowest, i.e., 1.9×10^6 cells.cm^{-3} and 47 µm, respectively. The low cell density value indicates that some of the TEMs have not been expanded, as also observed in Fig. 2(a-2). Also, the relatively low cell size is confirming that the TEMs have not expanded to their full potential at this low temperature. With an increase of the nozzle temperature to 200 °C, cell density and cell size both increased to 3.3×10^6 cells.cm^{-3} and 53 µm, respectively, indicating that a greater number of TEMs expanded and each TEM expanded to a greater degree. Further increase in the nozzle temperature to 225 °C did not cause any significant change in the cell density and cell size. Not a significant change in the cell density implies that the majority of the TEMs expanded at 200 °C. Moreover, as explained earlier, the cell size at 225 °C case was also not greater than that in the case of 200 °C, due to the shrinkage of the TEMs.

Fig. 3(b) provides the printed foams' bulk density with respect to the nozzle temperature. Overall, the density trends agree with the measured cell sizes and cell densities. With an increase in the nozzle temperature from 175 °C to 200 °C, the part density was lowered significantly from 0.95 to 0.67 g.cm^{-3}. However, with further increase in nozzle temperature to 225 °C, no significant change was observed in the density. It is noted that the part density reflects the overall weight reduction because of the cellular structure as well as the inter-bead voids, if any, present in the printed foams.

3.1.2. *Tensile properties vs. nozzle temperature*

Fig. 4(a-b) depicts the tensile properties of the printed foams with respect to the nozzle temperature. For 175 °C case, yield strength and Young's modulus were 27 MPa and 2340 MPa, whereas the strain-at-break and toughness were 4.6 % and 0.9 J.cm^{-3}, respectively. For 200 °C case, yield strength and Young's modulus dropped to 14 MPa and 1266 MPa, respectively, whereas strain-at-break and toughness

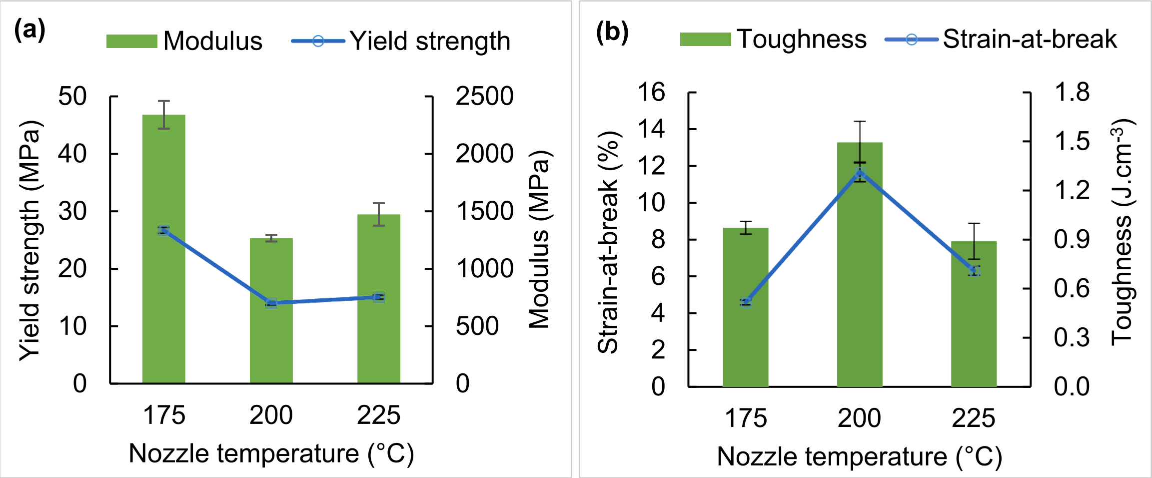

Fig. 4. (a) Yield strength and Young's modulus and (b) strain-at-break and toughness of the printed foams vs. nozzle temperature. The flow rate and print speed were 85 % and 25 mm.s^{-1}, respectively.

showed significant increases and were found to be 11.7 % and 1.5 J.cm^{-3}, respectively. For 225 °C case, yield strength and Young's modulus increased slightly and exhibited values of 15 MPa and 1473 MPa, respectively, whereas strain-at-break and toughness decreased significantly to 6.3 % and 0.9 J.cm^{-3}, respectively.

Overall, the tensile properties were impacted by both the bulk density as well as the microstructure of the foams. Yield strength and Young's modulus were primarily governed by the bulk density. At 175 °C, the bulk density was the highest and resulted in the largest yield strength and Young's modulus values [14,37,52–55]. The foams made at 200 °C and 225 °C had similar densities and thus provided similar yield strength and Young's modulus values. However, yield strength and Young's modulus for 225 °C case was slightly greater than those of 200 °C case, which may be attributed to a better raster-to-raster bonding due to the greater inter-molecular diffusions of PLA polymeric chains deposited at higher nozzle temperature [56]. The strain-at-break and toughness were maximum at 200 °C and dropped significantly in both 175 °C and 225 °C cases. The drop in the strain-at-break and toughness for the case of 175 °C is related to its high bulk density. In brittle polymeric foams such as PLA, usually strain-at-break and toughness decrease with an increase in the density [17,20]. The drop in the strain-at-break and toughness for the case of 225 °C is however primarily related to the morphology, as the two cases of 200 and 225 °C had similar densities. Larger cell size scatter, deformed cells, and the defective wrinkled shells all contributed to a reduction in the ductility of the foam. Wrinkled shells were not able to remain fully intact and transfer loads for longer times and could have acted as stress concentration locations for earlier catastrophic failure of the foams, causing the material to exhibit more brittle behavior.

3.2. *Effect of flow rate and print speed*

3.2.1. *Microstructure vs. flow rate and print speed*

Fig. 5(a-b-c) shows the internal microstructure of the printed foams at three different set flow rates of 55 %, 85 %, and 100 %, respectively. For the foams made at a flow rate of 55 %, the inter-bead gaps and raster boundaries were formed as evident in Fig. 5(a) and its inset. With an increase in the flow rate from 55 % to 85 %, the inter-bead mesostructural gaps vanished in the internal microstructure, and foam morphology became more homogeneous (Fig. 5(b)). However, with further increase of the flow rate to 100 %, the uniformity in the cellular morphology was found to slightly decrease (large cell pointed by the blue arrow in Fig. 5(c) inset) along with traces of unexpanded microspheres (yellow arrow in Fig. 5(c) inset).

Fig. 5(d-b-e) also shows the internal microstructure of the foams, printed at the speeds of 5, 25, and 125 mm.s^{-1}, respectively. In the parts printed at a speed of 5 mm.s^{-1}, the cellular morphology exhibited anomalies such as elongated or deformed cells (blue arrows in Fig. 5(d) inset) as well as defective shells with wrinkles (red arrows in Fig. 5(d) inset). Increase of the print speed to 25 mm.s^{-1} improved the internal microstructure. However, the highest speed of 125 mm.s^{-1} resulted in the formation of huge inter-bead gaps (Fig. 5(e)), highly nonuniform cellular structure in terms of distribution, shape, and size, as well as unexpanded microspheres (Fig. 5(e) inset).

The cell size, cell density, and bulk density of the foams all were affected by both the flow rate and print speed. As seen in Fig. 6(a), parts printed at a flow rate of 55 % had the largest cell size (57 μm) with the smallest cell density (1.25 × 10^{6} cells.cm^{-3}). As the flow rate was changed to 85 %, the cell size dropped to 51 μm and the cell density increased to 3.15 × 10^{6} cells.cm^{-3}. Further increase of the flow rate to 100 % resulted in opposite trends, i.e., the cell size slightly increased to 53 μm and the cell density decreased to 2.04 × 10^{6} cells.cm^{-3}. Moreover, Fig. 6(b) shows the printed foams' bulk density with respect to the flow rate. Once the flow rate was increased from 55 % to 100 %, the bulk density showed a continuous increase from 0.56 to 0.79 g.cm^{-3}.

As Fig. 6(c) shows, the foams printed at a speed of 5 mm.s^{-1} showed the highest cell size of 54 μm with the cell density of 1.52 × 10^{6} cells.cm^{-3}. With a change in the print speed from 5 to 25 mm.s^{-1}, the cell size decreased to 51 μm and the cell density increased to 3.15 × 10^{6} cells.cm^{-3}. Further increase in the print speed to 125 mm.s^{-1} resulted in the lowest values of the cell size, i.e., 46 μm and the cell density of 0.74 × 10^{6} cells.cm^{-3}. Part density showed no significant change when the speed was changed from 5 to 25 mm.s^{-1}. However, the part density was significantly increased to 0.94 g.cm^{-3}, when the highest speed, i.e.,

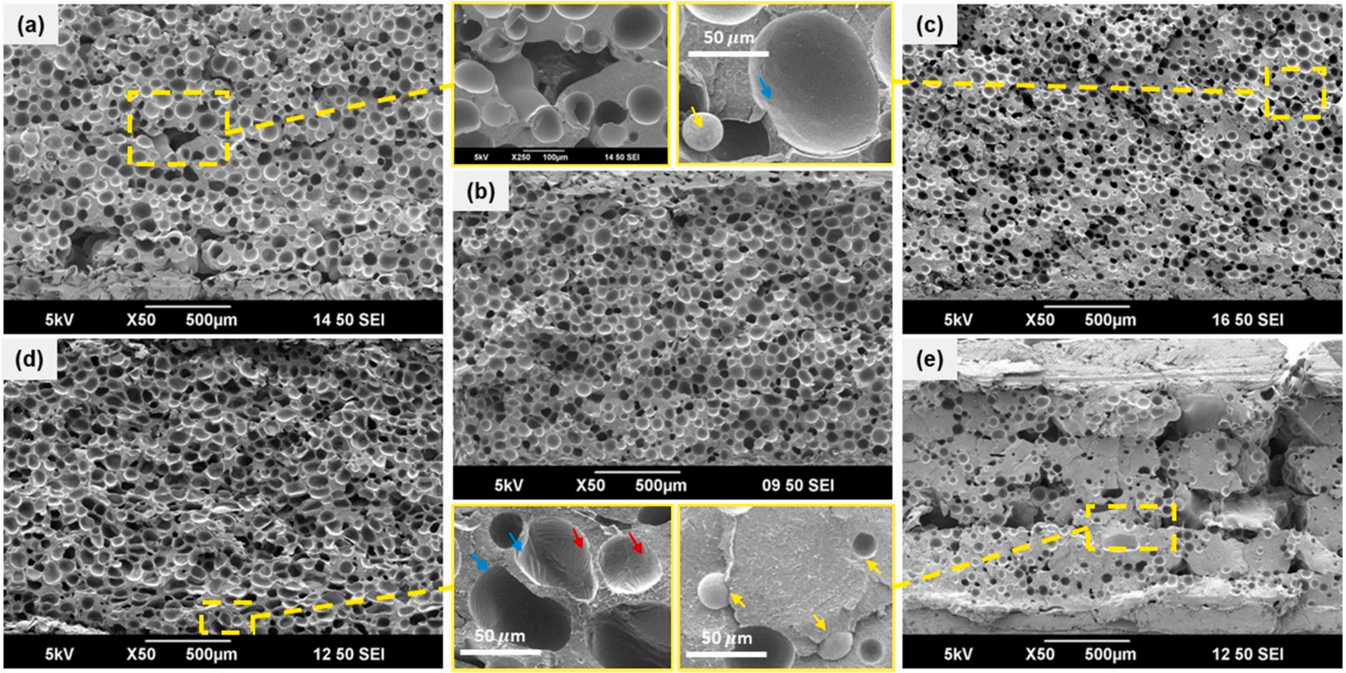

Fig. 5. Cellular morphologies of the printed foams at various flow rates and print speeds: flow rates of (a) 55 %, (b) 85 % and (c) 100 %, and print speeds of (d) 5 mm.s^{-1}, (b) 25 mm.s^{-1}, and (e) 125 mm.s^{-1}. (b) is same for 85 % flow rate and 25 mm.s^{-1} print speed. The nozzle temperature was 200 °C.

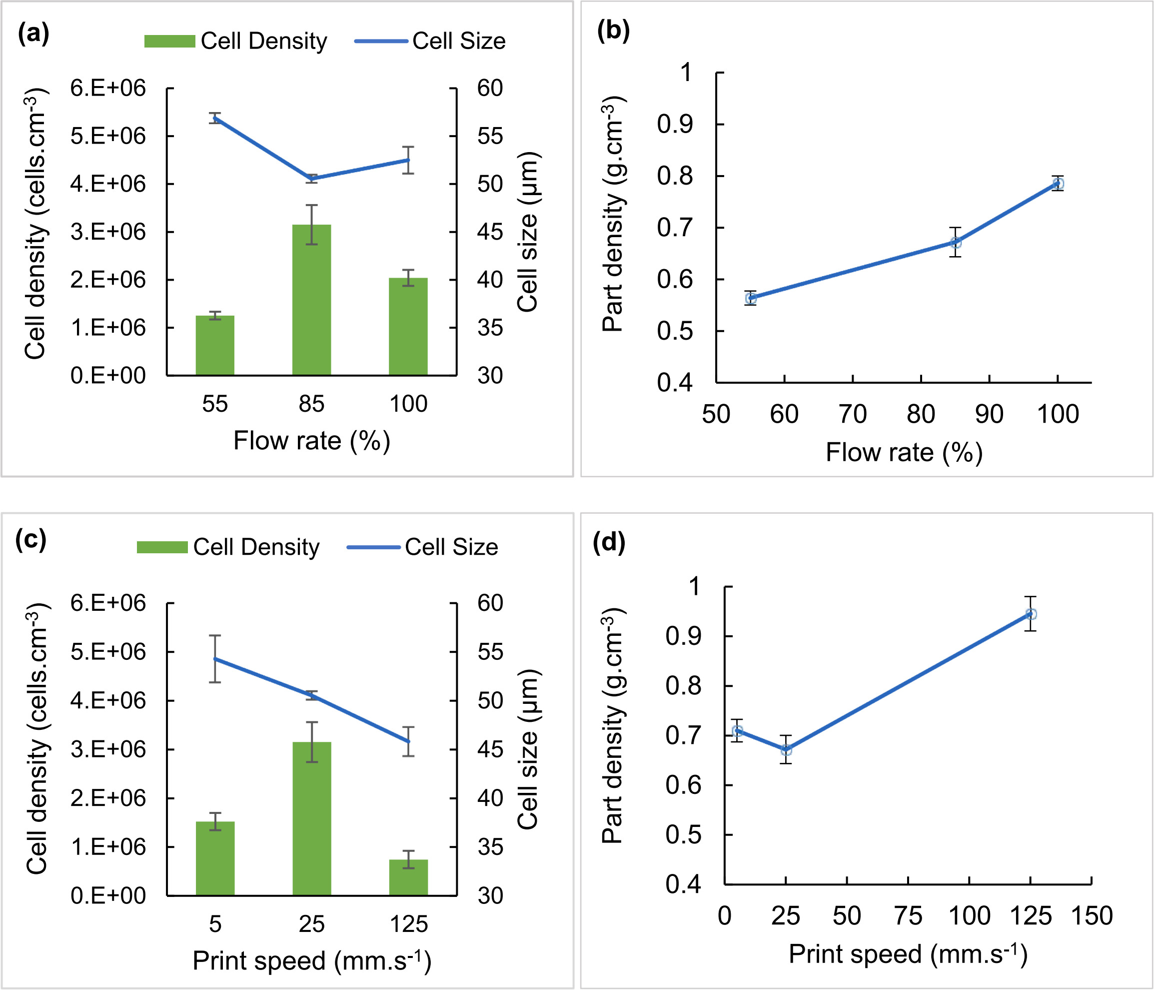

Fig. 6. Cell density, cell size, and part density of the printed foams as functions of (a-b) flow rate and (c-d) print speed at a print temperature of 200 °C.

125 mm.s^{-1} was used.

3.2.2. Residence time and nozzle throughput

With a close examination of the printing process, it can be found that both flow rate and print speed set points are controlled within the g-code by calculating the required filament feed-in velocity, U_I. For instance, to increase the flow rate or the print speed, U_I is increased in the program accordingly. With an increase in U_I, the melt travels faster and thus the residence time will decrease. The expansion of the microspheres is a time dependent phenomenon, and the microsphere size will enlarge with time, once a certain temperature range is obtained. The residence time can thus be used as an estimate of the time at which the microspheres are growing. Therefore, longer residence time translates into a longer time given for the TEMs to expand. Moreover, longer residence times will provide more time for the heat transfer from the nozzle to the melt, facilitating higher levels and/or more uniform distribution of the melt temperature. This in turn can facilitate further or more uniform growth of the TEMs. It should however be noted that excessively longer residence times can result in excessive gas loss through the TEM shell, causing a shrinkage in the microsphere due to pressure loss before shell solidification.

Therefore, one of the fundamental factors that may be used to correlate both the flow rate and the print speed to the foaming behavior is the residence time, t_r. Table 2 lists the t_r values obtained using both analytical and experimental approaches described in Section 2.3.3. When the flow rate is increased from 55 % to 100 %, t_r is reduced from 9.47 to 5.21 s. The range of residence time for print speed was even wider, i.e., from 29.42 to 1.32 s, corresponding to the speeds of 5 and 125 mm.s^{-1}, respectively.

Table 2
Filament feed-in velocity (U_I) and estimated residence time (t_r) at various flow rates and print speeds.

Flow rate (%)	Filament feed in velocity (U_I) (mm.s^{-1})	Residence time, t_r (s)	
		Analytical	Experimental
55	1.87	9.56	9.47 ± 0.02
85	2.87	6.22	6.02 ± 0.03
100	3.38	5.27	5.21 ± 0.05
Print speed (mm.s^{-1})			
5	0.58	30.94	29.42 ± 0.02
25	2.87	6.22	6.02 ± 0.03
125	14.43	1.24	1.32 ± 0.07

In addition to t_r, the volumetric throughput relative to the prescribed bead geometry is another important factor. Volumetric throughput is the available volume of the material per unit time that is used to fill the predetermined space (by the set print conditions) during the raster deposition. In the F-3DP process, this volumetric throughput depends not only on the process set parameters (e.g., flow rate) but also on the degree of the foam expansion before deposition.

The lowest flow rate of 55 % resulted in a relatively long residence time of 9.47 s (Table 2), giving enough time for the microspheres to expand, and thus providing the largest cell sizes (Fig. 6(a)) and the lowest part density (Fig. 6(b)). However, it also delivered the smallest throughput. The presence of the inter-bead gaps (Fig. 5(a)) denotes insufficient throughput of the foamed extrudate. Even with the volume increase due to the foam expansion, the amount of material per unit time supplied to form the raster was too low such that the inter-bead spaces could not be fully filled, leaving the inter-bead gaps behind. The lowest cell density for this case (Fig. 6(a)) can be attributed to the large amount of inter-bead free spaces, which do not contain microspheres. Upon increasing the flow rate from 55 % to 85 %, the residence time decreased, and the throughput increased (Table 2). Shorter residence time lowered the degree of expansion and caused a drop in the cell size (Fig. (6a)). Increase in the throughput resulted in a better filling during raster deposition and thus the inter-bead voids vanished (Fig. 5(b)). This also caused an increase in the cell density (Fig. 6(c)). At a flow rate of 100 %, the residence time was too short (5.21 s) resulting in some unexpanded microspheres (Fig. 5(c) inset) and a reduction in the cell density (Fig. 6(a)), with larger variation in the cell size. Lower t_r values are likely to create nonuniformity in the temperature distribution which will cause nonuniform expansion inside the polymer matrix along with higher probability of microspheres being in unexpanded state.

The longest residence time (29.42 s) was associated with the smallest print speed of 5 mm.s^{-1} (Table 2). Longer residence time did provide longer time for the expansion which resulted in larger cell size, but at the expense of morphological anomalies due to unwanted shrinkage of cells (Fig. 5(c)). As seen in Fig. 5(d), the anomalies such as wrinkled shells, deformed microspheres, and large variation in cell sizes are likely due to the excessively long residence time causing the gas loss and shrinkage of the already-expanded microspheres. On the other hand, the cell density was also not the highest which may be related to the collapse of some cells as a consequence of excessive gas loss. The part density was not the lowest and can be related to having a relatively low cell density. Increasing the speed to 25 mm.s^{-1} caused a reduction in the cell size and an increase in the cell density (Fig. 6(c)), which were due to the reduction of the residence time and increase of the throughput. The changes in the cell size and the cell density balanced out and the bulk density did not vary significantly. At the highest speed of 125 mm.s^{-1}, however, the morphology was changed significantly. This condition provided the lowest residence time of all the cases listed in Table 2, (i.e., 1.3 s). This residence time was too short such that some microspheres did not get enough heat to trigger and expand, as shown in the inset of Fig. 5(e). This short time resulted in the smallest cell size and cell density (Fig. 6(c)) for this case and consequently the highest part density. Moreover, a closer look at the morphology of Fig. 5(e) shows that most of the expanded cells reside at the exterior sections of the individual beads while their cores are relatively free of cells. As reported in [57], at higher print speeds or U_I, the temperature gradient inside the printer's barrel from the wall to the core can be relatively high. If the temperature difference is sufficiently large, it can create a gradient in the foam expansion as well. The melt is the hottest near the wall and the temperature was sufficient to cause the TEM expansion while the core did not experience sufficient time and temperature to activate the TEMs. It is believed that the temperature gradient in other cases was not severe enough to cause any measurable expansion gradient. Furthermore, unfilled regions with visible raster boundaries (Fig. 5(e)) were observed at this print speed which were due to the lack of sufficient expansion.

3.2.3. *Tensile properties vs. flow rate and print speed*

Overall, the tensile properties were also impacted by both the flow rate and the print speed. Fig. 7(a-b) shows the tensile properties vs. flow rate. All yield strength, Young's modulus, strain-at-break, and toughness increased as the flow rate was increased. One exception to this trend was a drop in strain-at-break, once the flow rate was raised from 85 % to 100 %, which resulted in only a mild increase in the toughness (Fig. 7(b)). The most significant increase was associated with the strain-at-break

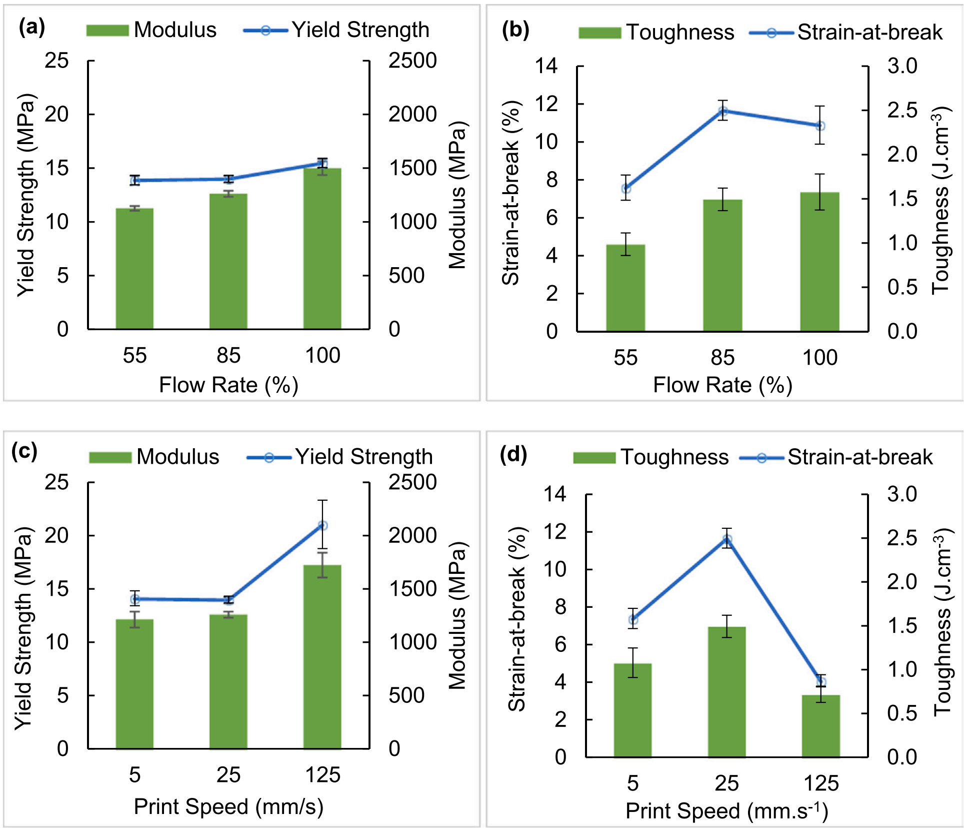

Fig. 7. Yield strength, modulus, strain-at-break, and toughness of the printed foams as a function of (a-b) flow rate and (c-d) print speed at a print temperature of 200 °C.

and toughness when the flow rate was increased from 55 % to 85 %. Fig. 7(c-d) also depicts the tensile properties vs. the print speed. The print speed and tensile properties exhibited somewhat similar trends to those of the flow rate and tensile properties; however, the speed's effects were more signified at high print speeds. In particular, the most significant changes were observed when the speed was raised from 25 to 125 mm.s^{-1}; yield strength and Young's modulus were increased by 50 % and 37 %, while strain-at-break and toughness reduced by 66 % and 52 %, respectively.

Overall, similar to the temperature case, it appears that yield strength and Young's modulus were mainly governed by the bulk density, but strain-at-break and toughness were significantly impacted by the microstructure. Looking at the tensile properties (Fig. 7(a) and (c)), there was not a significant difference in the yield strength and Young's modulus values when process parameters were changed from 55 % to 85 % flow rate or print speed from 5 to 25 mm.s^{-1}. With a change in the flow rate from 55 % to 85 %, due to an increase in the throughput, the part density increased slightly from 0.56 to 0.67 g.cm^{-3}, while a change in the print speed from 5 to 25 mm.s^{-1} did not cause a significant difference in the part density. However, improved cellular morphology with uniform and homogeneous cellular structure (and the absence of inter-bead gaps) enhanced the ductile behavior of the foams. Significant improvement in strain-at-break and toughness was observed (Fig. 7(b) and (d)). In the case of flow rate change, strain-at-break and toughness increased by 54 % and 52 %, respectively, whereas for the print speed change, strain-at-break and toughness increased by 58 % and 39 %, respectively.

At the flow rate of 100 %, due to a relatively higher part density, yield strength and Young's modulus values were found to be the highest for the flow rate cases (Fig. 7(a)). Moreover, the highest yield strength and Young's modulus values of all the cases of Table 2 were associated with the print speed of 125 mm.s^{-1} as it yielded the highest part density. In addition, the change in the flow rate from 85 % to 100 % did not cause a significant difference in the strain-at-break and toughness values, whereas the change in the print speed from 25 to 125 mm.s^{-1} caused a significant drop in the strain-at-break and toughness. This could be related to the significant raster underfilling as well as anomalies and nonuniformities observed in the microstructure (Fig. 5(e)).

3.3. Foam expansion limit

To study the overall process-density relation and find out the foam expansion limit, a process factor, P was defined as:

$$P = \frac{T_N - T_{\min}}{T_{\max} - T_{\min}} . \frac{t_r - t_{\min}}{t_{\max} - t_{\min}} \tag{7}$$

where T_N is the variable nozzle temperature and T_{max} and T_{min} are the maximum and minimum nozzle temperatures tested (Table 1). Similarly, t_r is the variable residence time and t_{max} and t_{min} are the maximum and minimum residence times tested (Table 1). Combining Eqs. (1), (2), (3), (5) and (7) defines P as a normalized factor that is a function of nozzle temperature, flow rate, and print speed. P can be viewed as a relative measure of the amount of energy provided to the system. $P = 0$ denotes the minimum temperature and minimum residence time, thus minimum relative energy, and $P = 1$ refers to the maximum temperature and maximum residence time, providing the maximum relative energy. Fig. 8 depicts the density vs. the process variable, P for all the foams obtained at various conditions. It is seen that with an increase in the process variable from $P = 0$ to about $P = 0.35$, denoted as Zone I in Fig. 8, the density decreases, which is related to the expansion of the microspheres. As discussed earlier, in this process window, as the temperature or time is increased, more energy is provided to the system and causes a further expansion of the microspheres and thus density decreases. The density reaches to a minimum value of about $\rho = 0.56$ g.cm^{-3} at $P = 0.35$. For a given material system, this corresponds to a maximum expansion of microspheres and thus the lowest achievable density.

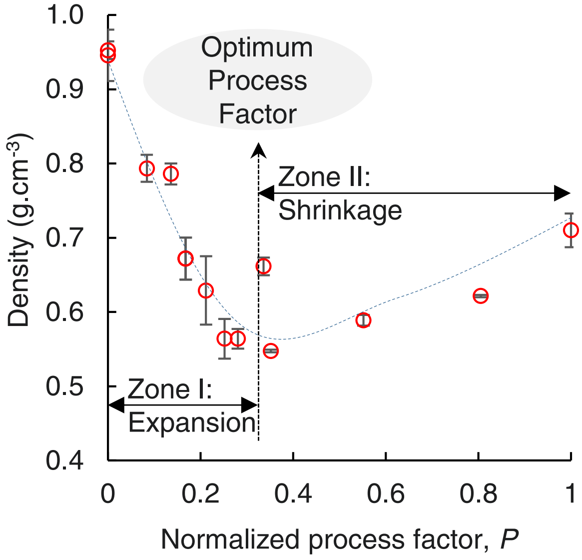

Fig. 8. Density as a function of the normalized process variable, P for all the foams obtained at various temperature, flow rate, and print speed conditions. T_N and t_r are nozzle temperature and residence time, respectively. The dashed curve is for visual guide.

As P was further increased beyond 0.35, denoted as Zone II in Fig. 8, the density started to rise. Zone II corresponds to the shrinkage of the microspheres due to gas loss which is signified as the process temperature and time increases. Therefore, it can be concluded that there is an optimum process condition that yields the maximum density reduction. Similar explanations in achieving the maximum density reduction via TEMs have also been reported previously in foam injection molding and extrusion processes [51,58]. It is also interesting to note that the density reduction in zone I occurred at a faster rate, compared to the rate of density rise in zone II. This is likely because the shrinkage of microsphere is a diffusion governed phenomenon and it takes longer time for the gas to diffuse out, as opposed to the pressure build up inside a closed shell of microsphere with time and temperature.

4. Conclusion

Process-microstructure-property relationships were investigated in detail for microcellular foams fabricated via MEX AM process. Expandable filament filled with TEM was used as the feedstock for in situ foaming during the MEX AM process. The impact of nozzle temperature, flow rate, and print speed on the cellular morphology, density, and mechanical behavior of the printed parts were investigated in detail. It was found that the residence time and temperature are the two key factors that govern the expansion and shrinkage of the microspheres inside the polymer melt and consequently dictates the cellular morphology of the foams. These two factors together with the volumetric throughput also control the mesostructure of the prints. Optimized residence time (controlled via flow rate and print speed) and temperature enabled the 3D printing of foams with maximum density reduction, uniform cellular morphologies, and void-free bead-to-bead interfaces, which resulted in the highest strain-at-break as well as toughness. The foam expansion/shrinkage behavior was observed and demonstrated as a function of a unified printing process factor, which combines temperature and residence time, derived from nozzle temperature, flow rate, and print speed. The results of this work shed light on understanding and advancing foam 3D printing process as a novel manufacturing approach with numerous applications.

CRediT authorship contribution statement

Karun Kalia: Writing – original draft, Methodology, Investigation, Formal analysis, Data curation. **Amir Ameli:** Writing – review & editing, Validation, Supervision, Resources, Project administration, Methodology, Funding acquisition, Formal analysis, Conceptualization.

Declaration of Competing Interest

The authors declare the following financial interests/personal relationships which may be considered as potential competing interests.

Acknowledgement

This work was supported by the United States National Science Foundation (NSF) under Grant Number 1822147 (Center for Science of Heterogeneous Additive Printing of 3D Materials (SHAP3D)) and the SHAP3D I/UCRC Members. Any opinions, findings, and conclusions or recommendations expressed in this material are those of the author(s) and do not necessarily reflect the views of the NSF or SHAP3D members. The authors would also like to thank NatureWorks LLC and Sekisui Chemical Co. Ltd. for providing the materials. Amir Ameli reports financial support was provided by National Science Foundation Industry-University Cooperative Research Centers Program.

References

[1] M. Sauceau, J. Fages, A. Common, C. Nikitine, E. Rodier, New challenges in polymer foaming: a review of extrusion processes assisted by supercritical carbon dioxide, Prog. Polym. Sci. 36 (2011) 749–766, https://doi.org/10.1016/j.progpolymsci.2010.12.004.

[2] M. Nofar, A. Ameli, C.B. Park, Development of polylactide bead foams with double crystal melting peaks, Polymers 69 (2015) 83–94, https://doi.org/10.1016/j.polymer.2015.05.048.

[3] L. Owolabi, Z. Mohamad, S. Fuad, S. Hashim, I. Dauda, Syntactic foams formulations, production techniques, and industry applications: a review, Integr. Med. Res. 9 (2020) 10698–10718, https://doi.org/10.1016/j.jmrt.2020.07.074.

[4] M. Li, J. Qiu, H. Xing, D. Fan, S. Wang, S. Li, Z. Jiang, T. Tang, In-situ cooling of adsorbed water to control cellular structure of polypropylene composite foam during CO_2 batch foaming process, Polymers 155 (2018) 116–128, https://doi.org/10.1016/j.polymer.2018.09.034.

[5] J. Pinto, D. Morselli, V. Bernardo, B. Notario, D. Fragouli, M.A. Rodriguez-Perez, A. Athanassiou, Nanoporous PMMA foams with templated pore size obtained by localized in situ synthesis of nanoparticles and CO_2 foaming, Polymers 124 (2017) 176–185, https://doi.org/10.1016/j.polymer.2017.07.067.

[6] D. Jahani, A. Ameli, P.U. Jung, M.R. Barzegari, C.B. Park, H. Naguib, Open-cell cavity-integrated injection-molded acoustic polypropylene foams, Mater. Des. 53 (2014) 20–28, https://doi.org/10.1016/j.matdes.2013.06.063.

[7] A. Ameli, M. Nofar, S. Wang, C.B. Park, Lightweight polypropylene/stainless-steel fiber composite foams with low percolation for efficient electromagnetic interference shielding, ACS Appl. Mater. Interfaces 6 (2014) 11091–11100, https://doi.org/10.1021/am500445g.

[8] W. Zhai, J. Jiang, C.B. Park, A review on physical foaming of thermoplastic and vulcanized elastomers, Polym. Rev. (2021) 1–47, https://doi.org/10.1080/15583724.2021.1897996.

[9] T.R. Kuang, H.Y. Mi, D.J. Fu, X. Jing, B.Y. Chen, W.J. Mou, X.F. Peng, Fabrication of poly(lactic acid)/graphene oxide foams with highly oriented and elongated cell structure via unidirectional foaming using supercritical carbon dioxide, Ind. Eng. Chem. Res. 54 (2015) 758–768, https://doi.org/10.1021/ie503434q.

[10] T. Sadik, C. Pillon, C. Carrot, J.A.Reglero Ruiz, Dsc studies on the decomposition of chemical blowing agents based on citric acid and sodium bicarbonate, Thermochim. Acta 659 (2018) 74–81, https://doi.org/10.1016/j.tca.2017.11.007.

[11] L.A. Mondy, M. Celina, J.M. Kropka, E. Russick, R.R. Rao, Design of chemically blown epoxy foams, in: Proceedings of the Twenty Seventh World Congr. Polym. Process. Soc. (2011).

[12] R.L. Heck, A review of commercially used chemical foaming agents for thermoplastic foams, J. Vinyl Addit. Technol. 4 (1998) 113–116, https://doi.org/10.1002/vnl.10027.

[13] R.Z. Zhang, J. Chen, M.W. Huang, J. Zhang, G.Q. Luo, B.Z. Wang, M.J. Li, Q. Shen, L.M. Zhang, Synthesis and compressive response of microcellular foams fabricated from thermally expandable microspheres, Chin. J. Polym. Sci. (Engl. Ed. 37 (2019) 279–288, https://doi.org/10.1007/s10118-019-2187-2.

[14] A. Kmetty, L. Katalin, Development of poly (lactide acid) foams with thermally expandable microspheres, Polymers (2020), https://doi.org/10.3390/polym12020463.

[15] V. Contreras, F.J. Maturana, J. Poveda, K.C. Núñez, J.C. Merino, J.M. Pastor, Optimization of injection parameters to obtain selected properties on foamed PP with hollow glass microspheres and thermally expandable microspheres using Taguchi method, J. Cell. Plast. (2020), https://doi.org/10.1177/0021955×20943097.

[16] A. Ameli, P.U. Jung, C.B. Park, Electrical properties and electromagnetic interference shielding effectiveness of polypropylene/carbon fiber composite foams, Carbon 60 (2013) 379–391, https://doi.org/10.1016/j.carbon.2013.04.050.

[17] A. Ameli, D. Jahani, M. Nofar, P.U. Jung, C.B. Park, Development of high void fraction polylactide composite foams using injection molding: mechanical and thermal insulation properties, Compos. Sci. Technol. 90 (2014) 88–95, https://doi.org/10.1016/j.compscitech.2013.10.019.

[18] H. Wu, G. Zhao, G. Wang, W. Zhang, Y. Li, A new core-back foam injection molding method with chemical blowing agents, Mater. Des. 144 (2018) 331–342, https://doi.org/10.1016/j.matdes.2018.02.043.

[19] H. Wu, G. Zhao, J. Wang, G. Wang, W. Zhang, Effects of process parameters on core-back foam injection molding process, Express Polym. Lett. 13 (2019) 390–405, https://doi.org/10.3144/expresspolymlett.2019.32.

[20] J.A.V. Jiménez, N. Le Moigne, J.-C. Bénézet, M. Sauceau, R. Sescousse, J. Fages, Foaming of PLA composites by supercritical fluid-assisted processes: a review, Molecules 25 (2020), https://doi.org/10.3390/molecules25153408.

[21] A. Ameli, M. Nofar, D. Jahani, G. Rizvi, C.B. Park, Development of high void fraction polylactide composite foams using injection molding: crystallization and foaming behaviors, Chem. Eng. J. 262 (2015) 78–87, https://doi.org/10.1016/j.cej.2014.09.087.

[22] J. Peng, Y. Srithep, J. Wang, E. Yu, L. Turng, X. Peng, Comparisons of micro-cellular polylactic acid parts injection molded with supercritical nitrogen and expandable thermo- plastic microspheres: Surface roughness, tensile properties, and morphology, J. Cell. Plast. (2012), https://doi.org/10.1177/0021955×12450208.

[23] S.T. Lee, C.B. Park. Foam Extrusion: Principles and Practice, second ed., CRC Press, Taylor & Francis Group, 2014.

[24] S.T. Lee, L. Kareko, J. Jun, Study of thermoplastic PLA foam extrusion, J. Cell. Plast. 44 (2008) 293–305, https://doi.org/10.1177/0021955×08088859.

[25] W. Gao, Y. Zhang, D. Ramanujan, K. Ramani, Y. Chen, C.B. Williams, C.C.L. Wang, Y.C. Shin, S. Zhang, P.D. Zavattieri, The status, challenges, and future of additive manufacturing in engineering, CAD Comput. Aided Des. 69 (2015) 65–89, https://doi.org/10.1016/j.cad.2015.04.001.

[26] P. Song, C. Zhou, H. Fan, B. Zhang, X. Pei, Y. Fan, Q. Jiang, R. Bao, Q. Yang, Z. Dong, X. Zhang, Novel 3D porous biocomposite scaffolds fabricated by fused deposition modeling and gas foaming combined technology, Compos. Part B Eng. 152 (2018) 151–159, https://doi.org/10.1016/j.compositesb.2018.06.029.

[27] B.K. Park, C.-J. Kim, D.E. Kwon, Y.-W. Lee, Design and fabrication of partially foamed grid structure using additive manufacturing and solid state foaming, Processes (2020), https://doi.org/10.3390/pr8121594.

[28] J. Wang, H. Xie, Z. Weng, T. Senthil, L. Wu, A novel approach to improve mechanical properties of parts fabricated by fused deposition modeling, Mater. Des. 105 (2016) 152–159, https://doi.org/10.1016/j.matdes.2016.05.078.

[29] M. Li, J. Jiang, B. Hu, W. Zhai, Fused deposition modeling of hierarchical porous polyetherimide assisted by an in-situ CO_2 foaming technology, Compos. Sci. Technol. 200 (2020), 108454, https://doi.org/10.1016/j.compscitech.2020.108454.

[30] S. Zhang, X. Shi, Z. Miao, H. Zhang, X. Zhao, K. Wang, J. Qin, G. Zhang, 3D printed polyurethane tissue engineering scaffold with hierarchical microcellular foam structure and antibacterial properties, Adv. Eng. Mater. (2022), https://doi.org/10.1002/adem.202101134.

[31] A.R. Damanpack, A. Sousa, M. Bodaghi, Porous PLAs with controllable density by FDM 3D printing and chemical foaming agent, Micromachines 12 (2021) 866, https://doi.org/10.3390/mi12080866.

[32] H. Andersson, J. Ortegren, R. Zhang, M. Grauers, H. Olin, Variable low-density polylactic acid and microsphere composite material for additive manufacturing, Addit. Manuf. 40 (2021), https://doi.org/10.1016/j.addma.2021.101925.

[33] A.Y. Kanani, A.E.W. Rennie, Additively manufactured foamed polylactic acid for lightweight structures, Rapid Prototype J. (2022), https://doi.org/10.1108/RPJ-03-2022-0100.

[34] J. Zhang, D. Li, W. Zhu, Y. Li, In situ 3D printing of poly-ether-ether-ketone / poly-ether-imide hierarchical cellular foams containing electromagnetic absorbent, Addit. Manuf. 59 (2022), 103181, https://doi.org/10.1016/j.addma.2022.103181.

[35] K. Zarybnicka, P. Lepcio, Effect of the nanoparticles on the morphology and mechanical performance of thermally blown 3D printed HIPS foams, Appl.Polym. (2022) 1–11, https://doi.org/10.1002/app.53413.

[36] B. Sun, L. Wu, Research progress of 3D printing combined with thermoplastic foaming, Front. Mater. (2022) 1–15, https://doi.org/10.3389/fmats.2022.1083931.

[37] A. Pawar, G. Ausias, Y.M. Corre, Y. Grohens, J. Férec, Mastering the density of 3D printed thermoplastic elastomer foam structures with controlled temperature, Addit. Manuf. 58 (2022), 103066, https://doi.org/10.1016/j.addma.2022.103066.

[38] K. Kalia, B. Francoeur, A. Amirkhizi, A. Ameli, In situ foam 3D printing of microcellular structures using material extrusion additive manufacturing, ACS Appl. Mater. Interfaces 14 (2022) 22454–22465, https://doi.org/10.1021/acsami.2c03014.

[39] K. Kalia, B. Francoeur, A. Amirkhizi, A. Ameli, Fabrication of expandable filaments towards in-situ foam 3D printing of microcellular poly (lactic acid), SPE ANTEC (2022).

[40] G. Gao, F. Xu, J. Xu, G. Tang, Z. Liu, A survey of the influence of process parameters on mechanical properties of fused deposition modeling parts, Micromachines 13 (2022) 1–28, https://doi.org/10.3390/mi13040553.

[41] J. Fernandes, A.M. Deus, L. Reis, M.F. Vaz, M. Leite, Study of the influence of 3D printing parameters on the mechanical properties of PLA, Proc. Int. Conf. Prog. Addit. Manuf. 2018-May (2018) 547–552, https://doi.org/10.25341/D4988C.

[42] M. Abouelmajd, A. Bahlaoui, I. Arroub, M. Zemzami, N. Hmina, M. Lagache, S. Belhouideg, Experimental analysis and optimization of mechanical properties of FDM-processed polylactic acid using Taguchi design of experiment, Int. J. Simul. Multidiscip. Des. Optim. 12 (2021), https://doi.org/10.1051/smdo/2021031.

[43] H. Li, T. Wang, Z. Yu, The quantitative research of interaction between key parameters and the effects on mechanical property in FDM, Adv. Mater. Sci. Eng. 2017 (2017), https://doi.org/10.1155/2017/9152954.

[44] M. Maiza, M.T. Benaniba, G. Quintard, V. Massardier-Nageotte, Biobased additive plasticizing Polylactic acid (PLA, Polimeros 25 (2015) 581–590, https://doi.org/10.1590/0104-1428.1986.

[45] X. Sun, M.A. Spalding, T.W. Womer, N. Uzelac, Design optimization of maddock mixers for single-screw extrusion using numerical simulation, in: Proceedings of the Annu. Tech. Conf. - ANTEC, Conf. Proc., 2017, 1017–1023.

[46] H.S. Podyman, Y.H. Dvoinos, V.A. Novik, Modeling the homogenization process of polyethylene compositions in a single-screw extruder with a Maddock mixing element, Mech. Compos. Mater. (2021) 517–526, https://doi.org/10.1007/s11029-021-09974-x.

[47] C. Hopmann, M. Schön, M.M. Reul, M. Facklam, A method for the validation of simulated mixing characteristics of two dynamic mixers in single-screw extrusion, Polymers) 12 (2020) 1–26, https://doi.org/10.3390/polym12102234.

[48] ASTM D638-14, Standard test method for tensile properties of plastics, ASTM Int. (2014) 1–17, https://doi.org/10.1520/D0638-14.

[49] ASTM D792-13, Standard test methods for density and specific gravity (relative density) of plastics by displacement, Am. Soc. Test. Mater. (2008) 6, https://doi.org/10.1520/D0792-20.

[50] M. Fujino, T. Taniguchi, Y. Kawaguchi, M. Ohshima, Mathematical models and numerical simulations of a thermally expandable microballoon for plastic foaming, Chem. Eng. Sci. 104 (2013) 220–227, https://doi.org/10.1016/j.ces.2013.09.010.

[51] Y. Kawaguchi, D. Ito, Y. Kosaka, M. Okudo, T. Nakachi, H. Kake, J.K. Kim, H. Shikuma, M. Ohshima, Thermally expandable microcapsules for polymer foaming—relationship between expandability and viscoelasticity, Polym. Eng. Sci. (2010), https://doi.org/10.1002/pen.21595.

[52] S. Wong, J.W.S. Lee, H.E. Naguib, C.B. Park, Effect of processing parameters on the mechanical properties of injection molded thermoplastic polyolefin (TPO) cellular foams, Macromol. Mater. Eng. 293 (2008) 605–613, https://doi.org/10.1002/mame.200700362.

[53] H. Kashani, Y. Ito, J. Han, P. Liu, M. Chen, Extraordinary tensile strength and ductility of scalable nanoporous graphene, Sci. Adv. 5 (2019) 2–7, https://doi.org/10.1126/sciadv.aat6951.

[54] J. Zhao, Q. Zhao, C. Wang, B. Guo, C.B. Park, G. Wang, High thermal insulation and compressive strength polypropylene foams fabricated by high-pressure foam injection molding and mold opening of nano-fibrillar composites, Mater. Des. 131 (2017) 1–11, https://doi.org/10.1016/j.matdes.2017.05.093.

[55] P. Li, B. Lan, Q. Zhang, Q. Yang, P. Gong, C.B. Park, G. Li, Microcellular foams simultaneous reinforcing and toughening strategy of combining nano-fibrillation network and supercritical solid-state foaming, Polymers 252 (2022), 124928, https://doi.org/10.1016/j.polymer.2022.124928.

[56] N. Aliheidari, J. Christ, R. Tripuraneni, S. Nadimpalli, A. Ameli, Interlayer adhesion and fracture resistance of polymers printed through melt extrusion additive manufacturing process, Mater. Des. 156 (2018) 351–361, https://doi.org/10.1016/j.matdes.2018.07.001.

[57] J. Zhang, E. Vasiliauskaite, A. De Kuyper, C. De Schryver, F. Vogeler, F. Desplentere, E. Ferraris, Temperature analyses in fused filament fabrication: from filament entering the hot-end to the printed parts, 3D Print. Addit. Manuf. 9 (2022) 132–142, https://doi.org/10.1089/3dp.2020.0339.

[58] M. Jonsson, O. Nordin, A.L. Kron, E. Malmstrom, Thermally expandable microspheres with excellent expansion characteristics at high temperature, J. Appl. Polym. Sci. 117 (2010) 384–392, https://doi.org/10.1002/app.31543.